Journal of Materials Chemistry B

Diblock Copolypeptoids: A Review of Phase Separation, Self-Assembly and Biological Applications

Journal:	*Journal of Materials Chemistry B*
Manuscript ID	TB-REV-02-2020-000477.R1
Article Type:	Review Article
Date Submitted by the Author:	01-May-2020
Complete List of Authors:	Xuan, Sunting; Lawrence Berkeley National Laboratory, Molecular Foundry Zuckermann, Ronald; The Molecular Foundry, Biological Nanostructures Facility

Diblock Copolypeptoids: A Review of Phase Separation, Self-Assembly and Biological Applications

Received 00th January 20xx,
Accepted 00th January 20xx

DOI: 10.1039/x0xx00000x

Sunting Xuan [a,b] and Ronald N. Zuckermann [a,b*]

Polypeptoids are biocompatible, synthetically accessible, chemically and enzymatically stable, chemically diverse, and structurally controllable. As a bioinspired and biomimetic material, it has attracted considerable attention due to its great potential in biological applications including drug and gene delivery, sensing, imaging, molecular recognition, and anti-cancer therapy. Diblock copolypeptoids, have especially been of increasing interest in the materials chemistry community because of their capacity to microphase separate and self-assemble to form a variety of nanoarchitectures. This review will discuss recent studies on diblock copolypeptoids regarding their synthesis, microphase separation, crystallization, self-assembly, and biological applications.

1. Introduction

Poly(*N*-substituted glycines) (a.k.a. polypeptoids) are a family of synthetic peptidomimetic polymers with the side chains appended to the nitrogen rather than the α-carbon. Compared to peptides, polypeptoids lack hydrogen bond donors and chiral centers along the backbones. This simple structure change endows polypeptoids with greatly enhanced chemical and enzymatic stability, excellent thermal processability, and good solubility in common solvents.[1-5] The reduced structural complexity of polypeptoids means that their properties are predominantly determined by the side-chain identity and monomer sequence, which simplifies their design and engineering. In addition, advances in both solution polymerization methods and the solid-phase submonomer synthesis method, have enabled ready access to a wide variety of well-defined polypeptoids, setting the stage for the development of polypeptoid materials for various biomedical and biotechnological applications.[1-3, 5, 6] Polypeptoids have shown promise as antibody mimetic scaffolds for molecular recognition[7-11], self-repairing membrane mimetics[12, 13], drug and gene delivery vehicles[14-18], templates for biomineralization[19], antifouling[20-23] and antimicrobial materials[24-26], imaging probes[27, 28], ligands for multimetallic clusters,[29] and tissue-engineering scaffolds[30]. Multiple review articles with particular emphasis on the synthetic methodologies, physicochemical properties, self-assembled nanostructures, and potential applications of polypeptoids have been published in recent years.[2-4, 6, 31-37] In recent years, diblock copolypeptoids, especially the ones with sufficiently different Flory Huggins parameter (χ), have attracted growing interest due to their capability to phase separate and assemble into various structures both in bulk and solution. This review will focus on the recent development of diblock copolypeptoids regarding their synthesis, phase separation, crystallization, self-assembly, and biological applications. Studies on diblock copolymers, containing a peptoid block and a polymer block (e.g., polystyrene and polyethylene oxide)[38-46] are beyond the scope of this review and will not be included.

2. Synthetic strategies

One remarkable advantage of polypeptoids is their synthetic accessibility, designability and precise structural tunability.[1, 2] Diblock copolypeptoids can be synthesized by submonomer solid-phase synthesis or ring-opening polymerization method depending on the degree of control over their structures and scalability.[1, 2] Comprehensive reviews regarding the synthesis of polypeptoids using solution polymerization method and submonomer solid-phase synthesis have been published.[1, 2, 4, 5] Thus, only a brief overview of the two methods will be described below.

2.1 Submonomer solid-phase synthesis

Zuckermann *et al*. initially developed the submonomer solid-phase synthesis to approach sequence-defined polypeptoids. The method involves a two-step monomer addition cycle in which the first step is an acylation reaction with bromoacetic acid, and the second step is a displacement reaction with a primary amine submonomer.[1, 47] Due to the readily availability and diversity of primary amines, polypeptoids with diverse side-chain and monomer sequence can be approached. The beauty of this method is that a wide variety of molecularly pure and nearly monodispersed polypeptoids (PDI ≈ 1) with precisely controlled length and sequences can be obtained for structure-property investigation and for a broad range of applications. A variety of sequence-defined diblock copolypeptoids bearing different side chains (e.g., aliphatic, aromatic, linear, branched and chiral) have been successfully synthesized by this method.[12, 48-56] The drawback of this method is that, due to the iterative nature of the synthesis, main chain lengths with DP > 50 are difficult to obtain.

2.2 Ring-opening polymerization method

Recent advances in controlled polymerization of *N*-substituted *N*-carboxyanhydride (R-NCA) monomers have enabled access to

[a] *Molecular Foundry, Lawrence Berkeley National Laboratory, Berkeley, CA 94720.*
[b] *Materials Sciences Division, Lawrence Berkeley National Laboratory, Berkeley, CA 94720*

Electronic Supplementary Information (ESI) available: [details of any supplementary information available should be included here]. See DOI: 10.1039/x0xx00000x

a variety of well-defined polypeptoids with relatively high molecular weight and low polydispersity.[2, 6, 57] Linear polypeptoids can be easily obtained by the controlled ring-opening polymerization (ROP) of R-NCA monomers using amines as the initiator.[5, 6] Luxenhofer *et al*. reported the successful synthesis of linear amphiphilic diblock copolypeptoids, poly(*N*-methyl glycine)-*b*-poly(*N*-butyl glycine) (PNMG-*b*-PNBG), with well-controlled molecular weight and narrow molecular weight distribution by sequential ROP of methyl-NCA and butyl-NCA using benzyl amine as the initiator.[58] They also demonstrated the living ROP of R-NCAs from amine functionalized solid supports.[59] The drawback of R-NCA monomers is their sensitivity to moisture that extremely anhydrous conditions are required. Ling *et al*. also reported the controlled ROP of a more stable monomer, *N*-substituted *N*-thiocarboxyanhydride (R-NTA), using benzyl amine as the initiator, to obtain amphiphilic diblock copolypeptoids, poly(*N*-3-(methylthio)propyl glycine)-*b*-polysarcosine (pMeSPG-*b*-pSar), with well-defined structures.[14] Controlled ROP of R-NCA was also realized using benzyl alcohol as the initiator and 1,1,3,3-Tetramethylguanidine (TMG) as the promoter.[60] Zhang *et al*. reported that well-defined cyclic polypeptoids can be approached through *N*-heterocyclic carbenes (NHCs) or 1,8-diazabicyclo[5.4.0]undec-7-ene (DBU)-mediated zwitterionic ring-opening polymerization (ZROP).[61, 62] Thus, diblock copolypeptoids with high molecular weight and relatively narrow molecular weight distributions can be synthesized by solution polymerization methods; however, their monomer sequences cannot be precisely controlled. Also, The R-NCA monomers need extremely anhydrous conditions due to their sensitivity to moisture.

Current peptoid synthesis methods are efficient enough to enable many areas of research, but there are still limitations that need to be overcome. The ability to synthesize even longer chains with increased chemical diversity, and precision sequence control is likely to remain a challenge for some time to come. However, efforts have been devoted to develop novel and improved synthetic strategies. Recently, the iterative Ugi reaction has been introduced to synthesize sequence-defined peptoids of limited length in solution.[63] Studies have shown that high molecular weight, sequence-defined peptoids (up to 100mers) can be obtained by the chemical ligation of two or more shorter strands, via the post-synthesis coupling of terminal-functionalized peptoids.[64] Others have combined solution and solid-phase techniques to create tailored, multi-block peptoids of controlled polydispersity.[65] Development of more efficient peptoid synthesis methodologies remains a fundamental challenge for the field.

3. Phase separation, crystallization and self-assembly of diblock-copolypeptoids

3.1 Diblock copolypeptoids synthesized by submonomer solid-phase synthesis

3.1.1 Amorphous amphiphilic diblock copolypeptoids

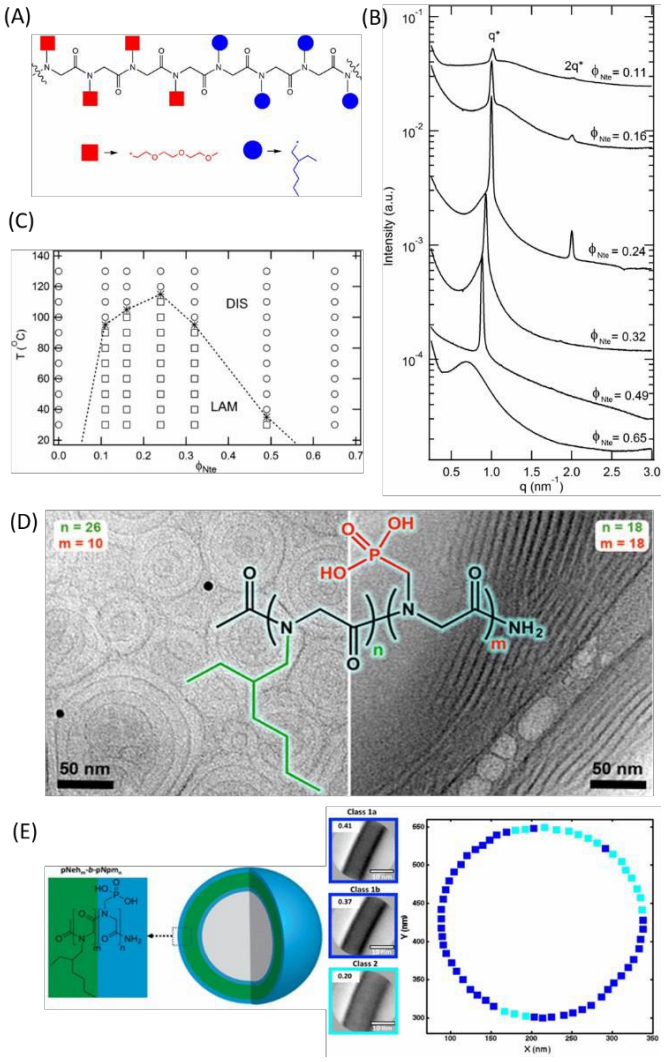

Figure **1**. Microphase separation of amorphous diblock copolypeptoids. (A) Schematic of pNte-*b*-pNeh. The blue circles represent pNeh, and the red squares represent pNte. (B) SAXS profiles at room temperature for pNte-*b*-pNeh with the same chain lengths while different volume fraction of Nte block. Profiles are vertically offset for clarity. (C) Phase diagram of pNte-*b*-pNeh at various temperatures and volume fractions of pNte (ϕ_{Nte}), where DIS is the disordered phase and LAM is the lamellar phase. (D) Energy filtered transmission electron microscopy (EFTEM) analysis indicates the various morphologies of the moisture annealed $pNeh_m$-*b*-$pNpm_n$ drop-casted thin films. (E) Averaged high-resolution electron micrographs of boxes extracted from vesicles after classification. Classes 1a and 1b have very similar membrane thicknesses (collectively class 1), whereas class 2 has a larger membrane thickness. The probability of finding each class in the four vesicles is given in the boxes. The locations of the boxes along the vesicle perimeter are shown, dark blue is class 1, whereas light green is class 2. (A-C). Adapted with permission from Ref. [49]. Copyright (2013) American Chemistry Society. (D). Reprinted with permission from Ref. [53]. Copyright (2016) American Chemistry Society. (E). Reprinted with permission from Ref. [66]. Copyright (2019) American Chemistry Society.

The diblock copolypeptoids synthesized by the solid-phase method are monodisperse and sequence-defined with atomically precise structures. The precise control over the chemical structure of diblock copolypeptoids allows systematic investigation of the effect of monomer sequence on their phase separation behaviour. Sun *et al*. reported a series of comb-like amphiphilic diblock copolypeptoids with nearly monodispersed molecular weight (PDIs ≤ 1.00013) , poly(*N*-2-(2-(2-methoxyethoxy)ethoxy)ethylglycine)-*b*-poly(*N*-(2-

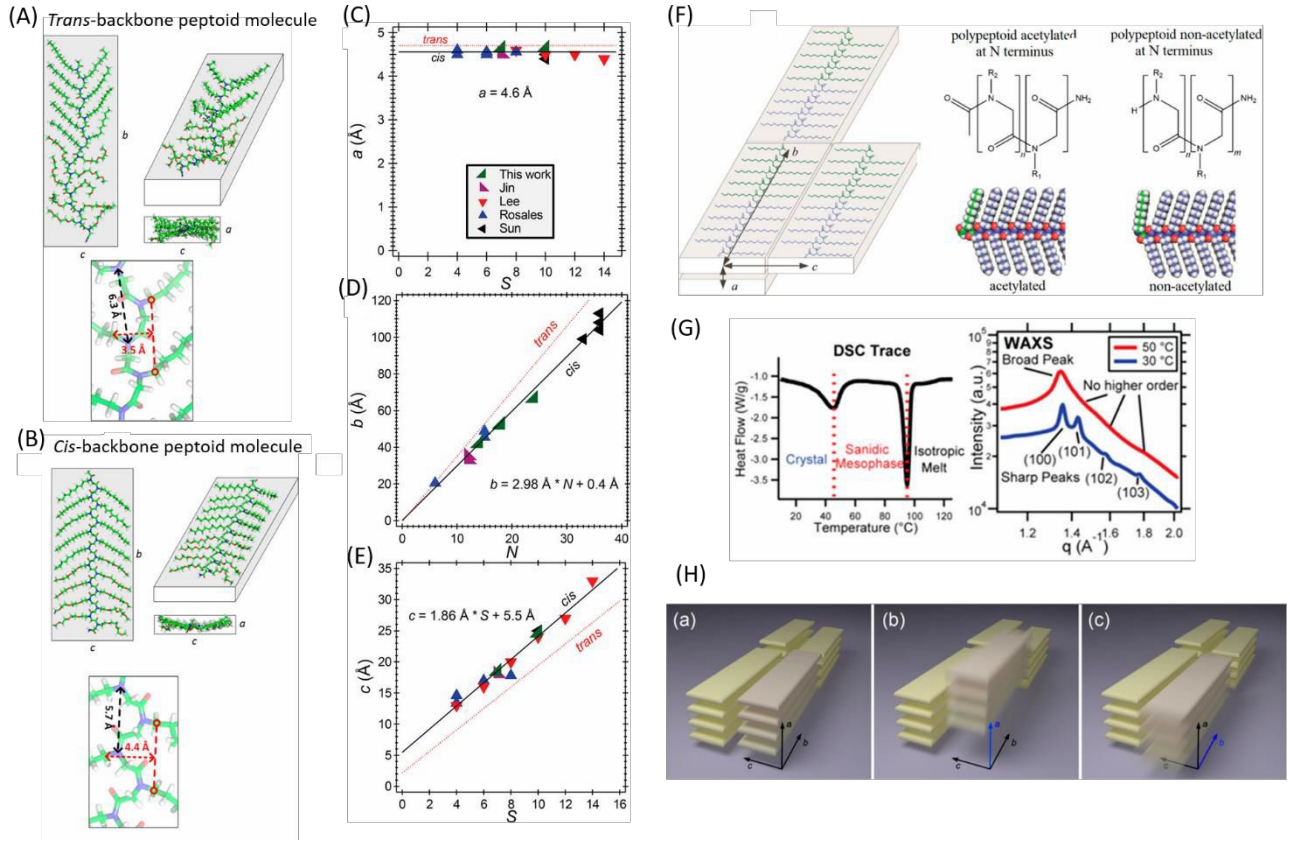

Figure **2**. Microphase separation of crystalline diblock copolypeptoids. (A, B) Relaxed molecular conformations *cis* and *trans* backbones. Each molecule is a representative taken from a 288-molecule MD simulation. (C, D, E) Collection of *a*, *b* and *c* dimensions taken from the X-ray scattering data. The side chain and main chain are denoted as *S* and *N*, respectively. (F) The unit cell and supramolecular assembly of Ac-pNdc$_9$-*b*-pNte$_9$ with the pNdc block in green and the pNte block in blue. And the chemical and geometric structures of acetylated and non-acetylated Ac-pNdc$_9$-*b*-pNte$_9$. (G) DSC and WAXS measurements of Ac-pNdc$_9$-*b*-pNte$_9$. (H) Comparison of ordering in Ac-pNdc$_9$-*b*-pNte$_9$ (a), the crystalline phase below T_{m1} and in (b) and (c), the sanidic liquid crystalline mesophase above T_{m1} and below T_{m2}. In the crystalline phase (a), the backbones are extended and parallel to each other. In the sanidic liquid crystalline mesophase, (b) and (c), the molecules stay aligned in stacks, and molecular distortions are restricted to the *ab* plane. (A-E). Adapted with permission from Ref. [68]. Copyright (2018) American Chemistry Society. (F-H). Adapted with permission from Ref. [54]. Copyright (2018) American Chemistry Society.

ethylhexyl)glycine) (pNte-*b*-pNeh) (Figure 1A), and studied their microphase separation behaviour using X-ray scattering techniques.[49] The hydrophobic pNeh block bearing branched alkyl side chains is amorphous and without any observable melting transitions. The chain length of the studied diblock copolypeptoids was held at 36 while the volume fraction of Nte block (ϕ_{Nte}) was varied from 0.11 to 0.65. All the compounds, except the one with ϕ_{Nte} = 0.65, phase-separated toa lamellar morphology, as evidenced by small angle X-ray scattering (Figure 1B). The experimentally determined order-to-disorder transition temperature exhibited a maximum at ϕ_{Nte} = 0.24, not ϕ_{Nte} = 0.5 as expected from theory (Figure 1C). These results are in disagreement with all known theories of microphase separation developed for block copolymers with polydispersity indices (PDIs) ranging from 1.01 to 1.10. This raises new questions about the intertwined roles of monomer architecture and polydispersity in the phase behaviours of diblock copolymers.

They also systematically studied the microphase separation of diblock copolypeptoids with the same abovementioned hydrophobic block and an anionic, hydrophilic phosphonated block, poly-*N*-(2-ethyl)hexylglycine-*b*-poly-*N*-phosphonomethylglycine (pNeh-*b*-pNpm), and demonstrated their ability to conduct protons, a desirable attribute for clean energy applications such as hydrogen fuel cells and artificial photosynthesis.[53] Similar to pNte-*b*-pNeh, the compounds studied all exhibited lamellar structures, as evidenced by the small-angle X-ray scattering. Interestingly, in contrast to the long-range lamellar structure observed for the hydrated film of pNeh$_{18}$-*b*-pNpm$_{18}$, a honeycomb morphology with an onion-like lamellar arrangement was observed by TEM for the hydrated film of pNeh$_{26}$-*b*-pNpm$_{10}$ (Figure 1D). In water, these phosphonated diblock copolypeptoids formed lipid-like vesicles with a spatial distribution of monolayer and bilayer packing morphologies within the single vesicle, as evidenced by low-dose cryogenic electron microscopy (cryo-EM) (Figure 1E).[66]

3.1.2 Crystalline amphiphilic diblock copolypeptoids with linear alkyl side chains

In contrast to the abovementioned polypeptoids bearing branched alkyl side chains which are amorphous, the polypeptoids bearing relatively long linear alkyl side chains are crystalline.[67] Greer *et al*. systematically investigated the microphase separation behaviour of crystalline diblock copolypeptoids bearing linear alkyl hydrophobic side chains and hydrophilic ethylene oxide side chains, varying side-chain length

and main chain length, by X-ray scattering and molecular dynamics (MD) simulation.[68] All the samples studied phase-separated into lamellar morphology with a rectangular crystal lattice (Figures 2F and H). Surprisingly, all the samples in this study, including 18 previously reported crystalline diblock copolypeptoids, all preferentially adopt an extended *cis*-backbone conformation (Figure 2B) with a uniform face-to-face packing spacing (~ 4.6 Å) along the *a* dimension, as evidenced by the unit cell dimensions obtained from X-ray scattering and MD simulations (Figures 2C-E). This is in contrast to the previous studies on isolated peptoid molecules in solution where there is a slight energetic preference for the *trans* conformation (Figure 2A). The *a* dimension for all the crystalline polypeptoids studied is always seen to be very close to 4.6 Å regardless of the side chain (Figure 2C). The *b* dimension increases linearly with the chain length (Figure 2D). The *c* spacing increases linearly with the side chain (*S*) (Figure 2E). The linear fits (solid black line) in all plots are consistent with an all *cis* backbone, and not the *trans* conformation. All the crystalline diblock copolypeptoids in this study exhibited two melting transitions based on differential scanning calorimetry (DSC) (Figure 2G). To assign the origin of the two thermal transitions, they studied the polymers by X-ray scattering at a variety of increasing temperatures.[54] They found that the lower thermal transition is associated with the distortions within the *ab* plane (Figure 2H), as evidenced by the broadening of the X-ray scattering peaks corresponding to the *a* spacings at 50°C, above the first thermal transition temperature (Figure 2G). The lower thermal transition was assigned to the melting of the crystal phase to a sanidic liquid crystalline phase while the higher thermal transition was attributed to the melting of the liquid crystalline phase to an isotropic phase (Figure 2G). Interestingly, the thermal transitions are strongly affected by the *N*-terminus of the hydrophobic block. Polypeptoids with an acetylated *N*-terminus exhibited two thermal transitions and sharp X-ray scattering peaks at high *q* corresponding to the *a* spacings at room temperature. However, polypeptoids with a free amine *N*-terminus (non-acetylated) exhibited only one thermal transition and broad X-ray scattering peaks corresponding to the *a* spacing at room temperature. This disorder is attributed to the difference in hybridization of the *N*-terminal amine atom (sp^3)

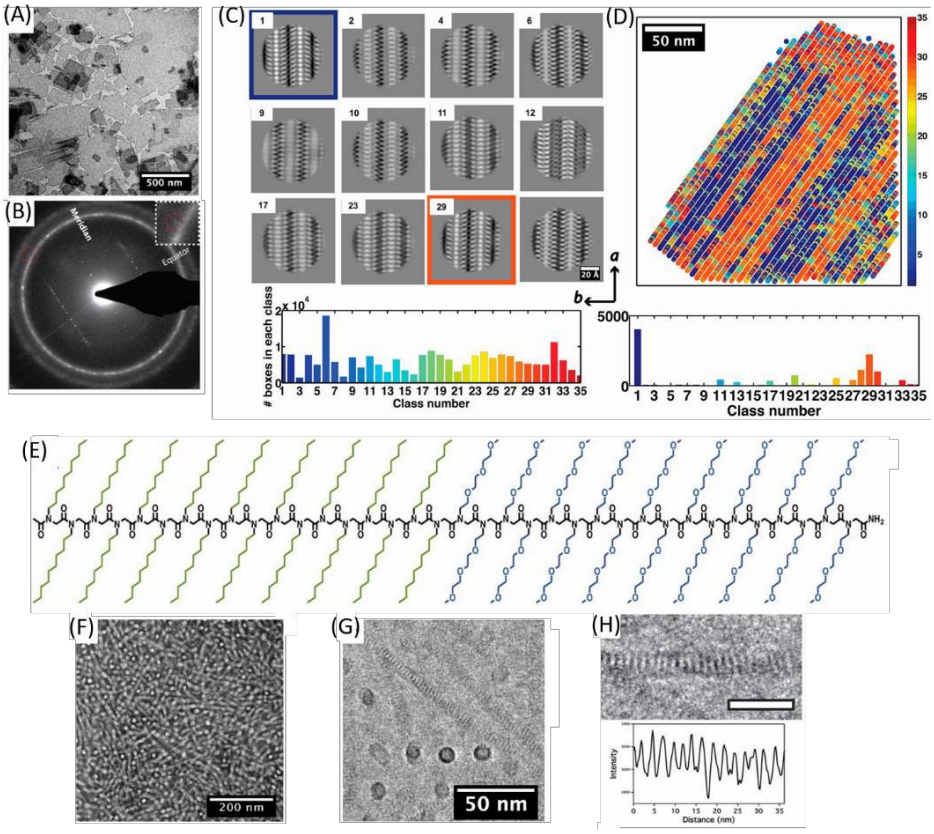

Figure **3**. Self-assembly of Ac-pNdc-*b*-pNte into nanosheets and nanotubes in water. (A) TEM micrograph of Ac-pNdc$_9$-*b*-pNte$_9$ nanosheets. (B) Cryogenic electron diffraction pattern of a vitrified hydrated Ac-pNdc$_9$-*b*-pNte$_9$ nanosheet; the brighter ring corresponds to gold 111 diffraction at 2.35 Å; inset red circle indicates (1, 19) reflection at 2.3 Å. (C) 12 dominant classes from 35 classes found in nanosheets. The histogram below shows the population of each of the 35 classes. (D) Distribution of classes in one micrograph. The two major classes, 1 and 29, are mirror images of each other. The histogram below shows the population of classes in this image. (E) Chemical structure of Ac-pNdc$_{18}$-*b*-pNte$_{18}$. (F) Uranyl acetate negative-stained TEM micrograph of dried nanotubes. (G) Cryo-EM 2D projection image shows nanotubes of uniform diameter in a vitrified thin film. (H) Cryo-EM close-up of a single nanotube (scale bar, 20 nm) shows regular latitudinal stripes (Top). A line profile along the longitudinal direction of the nanotube indicates a periodicity of 2.4 ± 0 .2 nm (Bottom). (A-D). Adapted with permission from Ref. [71]. Copyright (2018) American Chemistry Society.

which distorts the spatial positioning of the side chain relative to the internal side chains (sp^2) (Figure 2F).

They further explored the lithium ion conductivity of these diblock copolypeptoids. They systematically compared the lithium ion conductivity of the amorphous pNte-*b*-pNeh with that of the analogous crystalline pNdc-*b*-pNte sample containing the same hydrophilic pNte block that dissolves the salt and conducts ions. They demonstrated that the crystalline pNdc-*b*-pNte and amorphous pNte-*b*-pNeh, which both phase-separated into lamellar morphology, exhibited comparable conductivities.[50]

X-ray scattering, as mentioned above, is a common technique widely used in the characterization of phase-separation and crystallization of diblock copolymers. This technique, nevertheless, lacks the capacity to provide atomic details of the phase-separated structures in position space. Low-dose cryo-TEM has evolved to be an ideal technique to directly image soft-material structures though many challenges remained. Hard materials such as metals are stable to electron beam exposure that individual atoms are possible to be resolved under high-dose conditions. Soft materials, such as biological macromolecules (e.g., protein) which are mainly composed of light atoms C, H, O and N, are very sensitive to electron beam exposure and weakly electron scattering, making them challenging to obtain high-resolution structures. Thus, low-dose of electron beam has to be used for soft materials to minimize beam damage to samples. Cryo-TEM won the 2017 Nobel prize in Chemistry for its outstanding contribution to the understanding of biological structures using the single-particle method of analysing and aligning numerous low signal-to-noise ratio images obtained under low-dose conditions.[69, 70] Taking advantage of the advances in low-dose cryo-TEM and the precisely-controlled feature of peptoid synthesis, self-assembled structures of diblock copolypeptoids have been directly imaged using low-dose cryo-TEM to obtain atomic details in position space (*vide infra*).

The crystalline diblock copolypeptoids, pNte-*b*-pNdc, can self-assemble into either crystalline nanosheets or nanotubes in water (Figure 3).[52, 71] Ac-pNdc$_9$-*b*-pNte$_9$, with acetylated *N*-terminus, was shown to self-assemble into two-dimensional (2D) crystalline nanosheets in water, as shown in Figure 3A.[71] Low-dose cryo-TEM was used to understand the crystal packing of the nanosheet at the atomic level. Combining the crystallographic and single-particle methods, Downing *et al*. observed, for the first time, crystalline grains and grain boundaries of the nanosheet made of Ac-pNdc$_9$-*b*-pNte$_9$ at the atomic level, showing the capability of cryo-TEM to image heterogeneity of synthetic polymer crystals.[71] The electron diffraction of a vitrified nanosheet displayed a prominent 25 Å repeat along the meridian in Figure 3B, which was attributed to the spacing of adjacent rows of backbones. Diffraction spots extend along rows parallel to the meridian was assigned to a distance corresponding to 4.6 Å, the face-to-face packing dimension. However, more detailed structural information could not be obtained due to the low signal-to-noise ratio of the nanosheet in low-dose cryo-TEM. Thus, they combined the crystallographic and single-particle methods to increase signal-to-noise ratio. Briefly, the electron micrographs obtained from low-dose cryo-TEM were divided into small boxes comprising crystal unit cells, which were then classified and averaged to reveal the shape and positioning of individual chains. 35 classes of unit cell were found using this method and 12 dominant classes were shown in Figure 3C. The histogram showed that the most highly populated classes are classes 1 and 29. Figure 3D showed the distribution of the 35 classes in one nanosheet micrograph. This method enables the direct visualization of heterogeneity in polymer crystal lattice. Due to the substantial heterogeneity of the nanosheets in this study, the atomic model matching the major crystal class in Figure 3 has not been established.

Their following work studied the effect of self-assembly conditions and the polymer end group structure on the crystalline ordering within the nanosheets.[72] The cryo-TEM images revealed enhanced long-range order by slowing down the self-assembly process at low temperature (4°C). The adjacent rows of polypeptoid molecules adopt either a predominantly parallel V-shaped packing or a predominantly anti-parallel V-shaped packing geometry. The inherent mechanisms causing these different crystal packings in the nanosheets have not been clearly elucidated.

Interestingly, Sun *et al*. reported that the Ac-pNdc-*b*-pNte, with longer chain lengths, formed crystalline nanotubes of uniform diameter instead of nanosheets (Figure 3E-G).[52] Stripes with 2.4 nm adjacent spacing along the tube axis, corresponding to the adjacent rows of backbones, were clearly observed by cryo-TEM (Figure 3H). This spacing (2.4 nm) is) is nearly the same as that observed in the Ac-pNdc$_9$-*b*-pNte$_9$ nanosheet, suggesting their similar packing between adjacent rows of backbones. A full mechanistic understanding of the self-assembly pathway and the inherent structure of the nanotubes is still under investigation.

Taking advantage of the sequence-controlled submonomer solid-phase synthesis, Zhang *et al*. reported a series of ionic diblock copolypeptoids where the total number (1 or 3) and position of ionic monomers (Nce) were precisely controlled

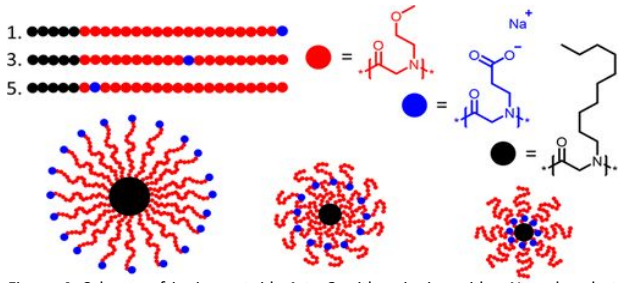

Figure **4**. Scheme of ionic peptoids **1** to **3** with anionic residue Nce placed at different positions and the cartoons of the corresponding formed spherical micelles showing the position of residue Nce in blue. Reprinted with permission from Ref. [56]. Copyright (2018) American Chemistry Society.

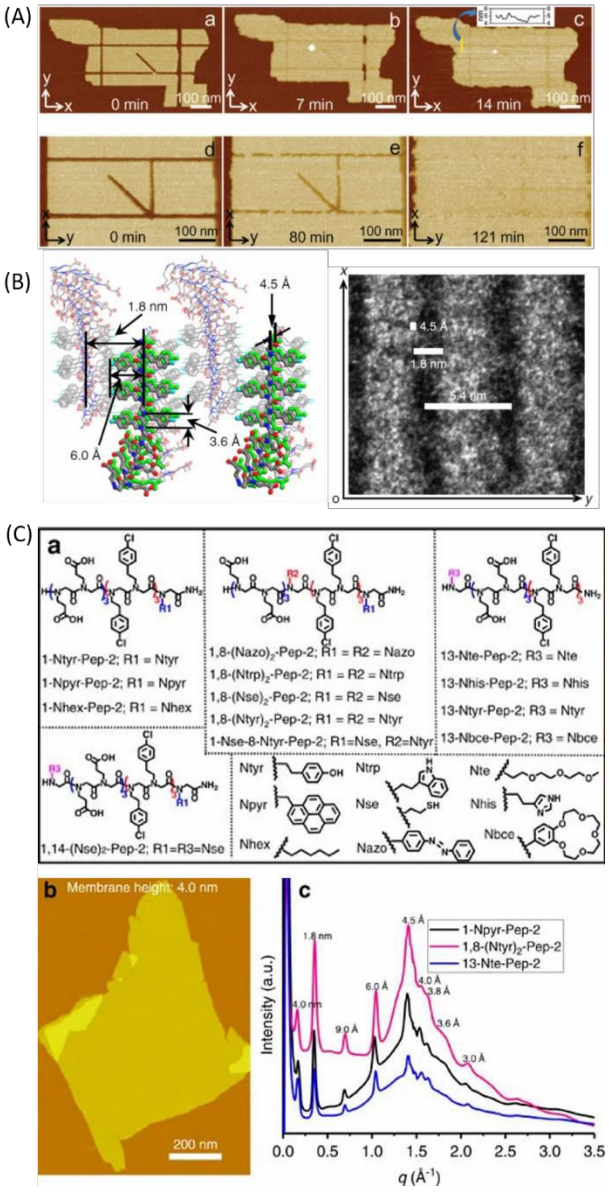

Figure **5** Self-assembly of pNce-*b*-pN4-Clpe into nanosheets. (A) In situ AFM images at different time points showing repair of nanosheet membranes on mica using polypeptoid solutions. Reprinted with permission from Ref. [13]. Copyright 2016 John Wiley and Sons. (B) Molecular model showing proposed packing of nanosheet and a high-resolution TEM image showing well-aligned strips in the nanosheet structure. (C) Tolerance of polypeptoid membrane structures to incorporation of functional objects. (a) Chemical structures of polypeptoids containing a wide range of functional objects. (b) AFM image of one 2D nanosheet assembled from 1-Npyr-Pep-2. (c) X-ray diffraction data of nanosheets assembled from 1-Npyr-Pep-2, 1,8-(Ntyr)2-Pep-2 and 13-Nte-Pep-2 are similar to the X-ray diffraction data of Pep-2, which shows that the core structure is retained. (B) and (C). Adapted from Ref. [12] under CC BY.

along the polymer chain of poly(*N*-decyl glycine)-*b*-poly(*N*-methoxyethyl glycine) (pNdc-*b*-pNme) (Figure 4).[56] Small-angle neutron scattering (SANS) analysis revealed that the micellar aggregation number (Nagg) and the micellar radius (Rm) both increase as the ionic monomer is positioned progressively away from the junction of the hydrophobic and hydrophilic blocks along the polymer chain (Figure 4), demonstrating the capability to precisely tailor the structure of small spherical micelles by controlling the sequence and position of the ionic monomer along the polymer chain.

3.1.3 Crystalline amphiphilic diblock copolypeptoids with aromatic side chains

Polypeptoids containing 2-phenylethyl side chains is another commonly used building block that is known to strongly promote crystallinity through π-π and hydrophobic interactions. Chen *et al*. reported the self-assembly of relatively short diblock copolypeptoids bearing a hydrophilic *N*-(2-carboxyethyl)glycine (pNce) block and a hydrophobic *N*-[2-(4-chlorophenyl)ethyl]glycine(pN4-Clpe) block, into membrane-mimetic crystalline and free-standing 2D nanosheets through a facile crystallization process (Figure 5).[12, 13] The structure of the nanosheets were analysed by TEM, AFM and X-ray scattering. The nanosheets showed a similar packing structure as that in the Ac-pNdc$_9$-*b*-pNte$_9$ nanosheets[71]. Stripes corresponding to the adjacent rows of backbones were clearly observed by TEM (Figure 5B). The self-repair ability of these nanosheets was demonstrated by *in situ* atomic force microscopy (AFM). Damage created in the nanosheets by the AFM tip was repaired upon addition of free polypeptoid in solution, allowing the creation of nm-sized patterns of distinct functional group domains within the nanosheets (Figure 5A). They further demonstrated the use of the nanosheets as a robust platform to incorporate and pattern functional moieties by introducing a variety of functional groups to the *N*-terminus or the side chains of the hydrophilic block and/or by co-crystallization approaches (Figure 5C). The structure of nanosheets were maintained upon incorporating a variety of functional moieties to the diblock copolypeptoids, as evidenced by the AFM and X-ray scattering (Figure 5C). To further understand and engineer the atomic-level structure of the self-assembled nanosheets, Xuan *et al*. studied a series of crystalline diblock copolypeptoids, by a combination of sequence-controlled synthesis, cryo-TEM, and MD simulations.[73] The diblock copolypeptoids were decamers containing a same hydrophilic pNte block and a series of *N*-2-phenylethylglycine-based hydrophobic blocks bearing a systematic series of aromatic ring substituents, varying in size and electron withdrawing or donating character (Figure 6). The amphiphilic diblock copolypeptoids formed free-floating 2D monolayer nanosheets in water (Figure 6A), in which not only individual polymer chains but also their relative packing orientations could be directly visualized by cryo-TEM (Figure 6B). Furthermore, bromine atom *para*-substituents at the side chains could be directly observed by cryo-TEM (Figure 6B), revealing atomic details in position space inaccessible by conventional scattering techniques. Surprisingly, the polypeptoid molecules shared the same backbone conformation in the nanosheets regardless of their different side-chain substituents. All the nanosheets studied formed a similar rectangular crystal lattice; however, they adopt different internal lattice packing geometries. Either parallel or anti-parallel packing of adjacent rows in nanosheet crystals were observed depending on the *para*-substituents of aromatic side chains which dominate the inter-row interactions in the *c*

direction. Initial studies indicated that neither the steric nor the electrostatic character of *para* substituents dominated the packing orientation of adjacent rows (parallel or anti-parallel). Further investigation is underway to probe the origin of the different packing. Interestingly, the MD simulations indicated that the inherently achiral polypeptoid *cis* backbone adopts a chiral conformation in the lattice, such that alternating rows pack with opposite backbone chirality. This phenomenon is currently under investigation by cryo-TEM 3D reconstruction of the nanosheets and polarized X-ray scattering. These atomic-level insights of polypeptoid crystals will direct the rational design of bioinspired nanomaterials with more precisely controlled structures and properties.

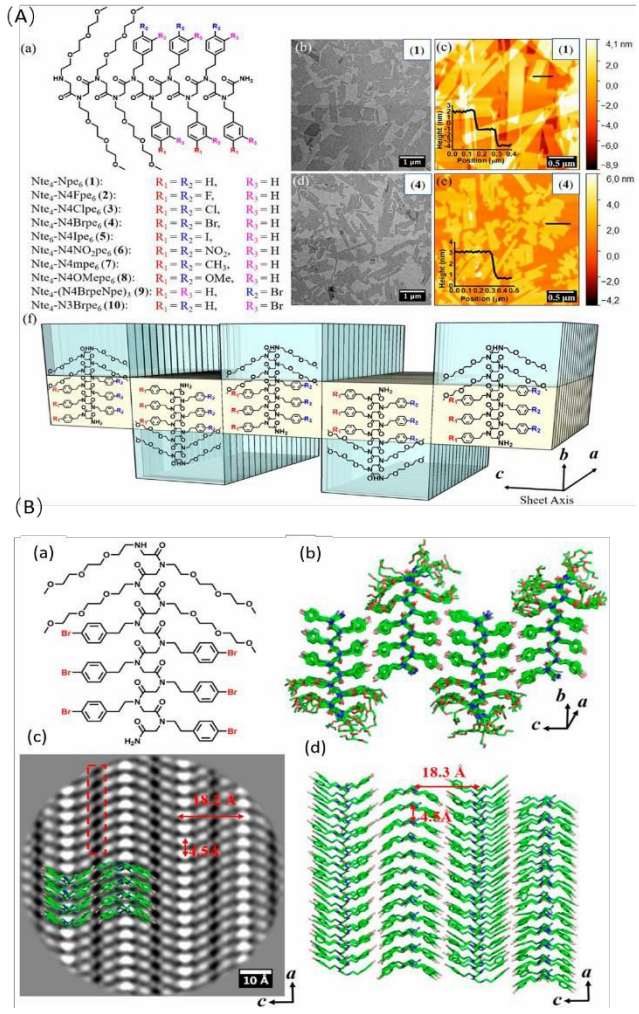

Figure **6**. Self-assembly and atomic structure nanosheets. (A) Self-assembly of diblock copolypeptoids into nanosheets. (a) Chemical structures of diblock copolypeptoids. (b, d) Representative TEM images of nanosheets. (c, e) Representative AFM images of nanosheets. (f) Proposed nanosheet structures: peptoid chains are packed antiparallel along the c direction and parallel along the *a* direction. (B) atomic structure of nanosheets. (a) Chemical structure of Nte_4-N4$Brpe_6$ (**4**). (b) Molecular model of sheet 4. The molecules are packed antiparallel along c direction and parallel along a direction. (c) Cryo-TEM image of sheet 4 from b direction (top view) showing antiparallel V shapes along the c direction. The Br atoms show a tip-to-tip packing (red box). (D) Top view of the hydrophobic domain in B from b direction showing antiparallel V shapes along the *c* direction. The structure is overlapped with cryo-TEM image shown in C.

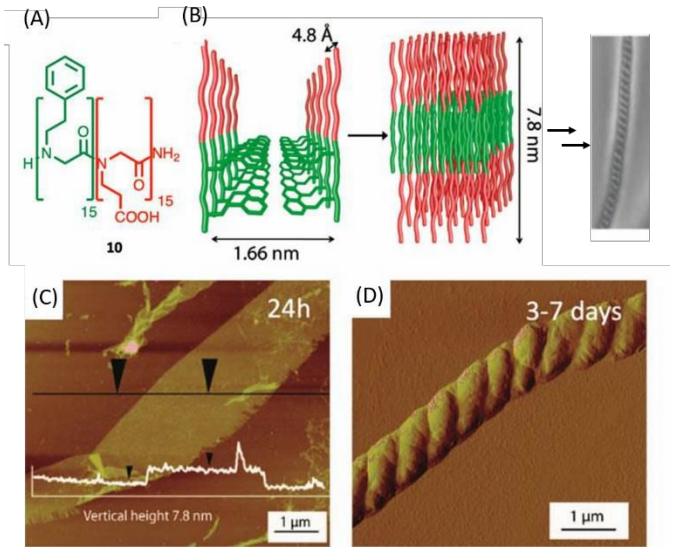

Figure **7**. Self-assembly of Npe_{15}-*b*-Nce_{15} into homochiral super helices. (A) Chemical structure of the diblock copolypeptoids. (B) Proposed self-assembly process into super helices. The peptoid chains initially packed into nanosheets as shown in (C) and subsequently transformed to super helices as shown in (D). Adapted with permission from Ref. [48]. Copyright (2010) American Chemistry Society.

Interestingly, Murnen *et al*. found that longer amphiphilic diblock copolypeptoid with the same pNpe block, $pNpe_{15}$-*b*-$pNce_{15}$, initially formed the nanosheet structure and subsequently transformed to homochiral left-handed superhelices (Figure 7).[48] The polypeptoids made up the superhelices are inherently achiral, making the observed homochiral superhelices an unusual and interesting result. The left-handed homochirality was shown to be remarkably robust as ether incorporation of chiral side chains or addition of chiral counterion could not change the overall superhelix chirality. The self-assembly of the superhelices was proposed to be lamellar stacks rolling up to form superamolecular double helical structure with the internal ordering of stacks being mediated by crystalline aromatic side chain interactions. The interplay of ionic interactions and hydrogen bonding of the carboxyethyl side chains were found to be critical to the formation of superhelices. At high pH (pH>9.5), only the sheet structures maintained due to the high level of deprotonation of the carboxylic acids and the resulting electrostatic repulsion. At a pH less than 5.5, the molecule is not soluble and no organized self-assembly occurs. Replacement of the ionic and hydrogen bonding pNce block with a hydrogen bonding but nonionic poly(*N*-(2-carboxamidoethyl)glycine) or an analogous nonionic and non-hydrogen bonding poly(*N*-(2-methoxyethyl)glycine) failed to form organized structures. The driving force and exact principle behind the formation of the homochiral superhelices have not yet been clearly elucidated.

Remarkably, Chen *et al*. reported that diblock copolypeptoids with the same hydrophilic pNce block while a hydrophobic block bearing 4-bromobenzyl side chains formed single-walled stiff nanotubes transformed from intermediate nanosheet structure. The cryo-TEM image clearly showed the tubular structure with high contrast dark walls and a low contrast bright

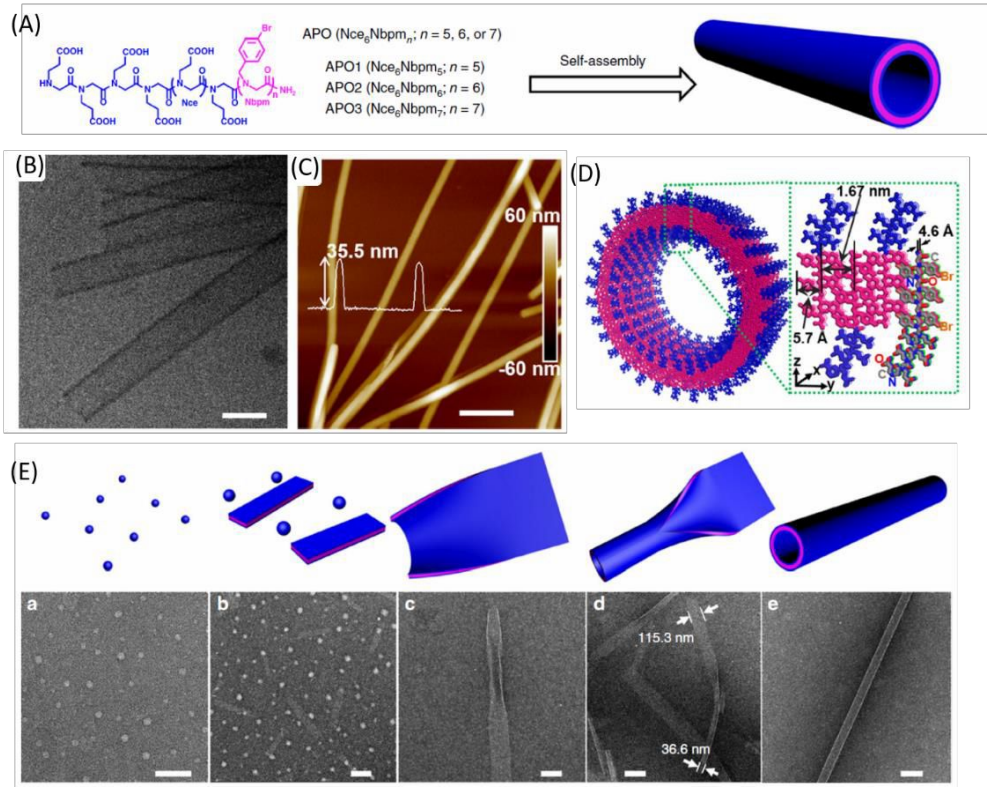

Figure **8**. Self-assembly of amphiphilic diblock copolypeptoids into stiff nanotubes. (A) Chemical structures of diblock copolypeptoids assembled into nanotubes. (B, C) TEM and AFM images of nanotubes, respectively. (D) A proposed model showing the molecular packing in nanotubes. (E) Time-dependent TEM images showing the assembly pathway of nanotubes: (a) immediately after dissolving, (b) after 0.5h crystallization, (c)after 24h crystallization, (d) after 48h crystallization, (e) after 72h crystallization. Adapted from Ref. [55] under CC BY.

channel (Figure 8).[55] The wall thickness and diameter of the nanotubes obtained from cryo-TEM were ~3.1 nm and 35 nm, respectively, much larger than the nanotubes (d = 9.3 ± 0.3 nm) made of Ac-pNdc$_{18}$-*b*-pNte$_{18}$ reported by Sun *et al*.[52] The wall thickness of the pNce-*b*-pNbpm nanotubes is similar to the thickness of the bilayer-like nanosheets they previously reported[12]. They proposed that the nanotubes were assembled through a unique "rolling up and closure of nanosheet" mechanism, as evidenced by intermediate nanoribbons with partially rolled up edges in captured by a cryo-TEM time series (Figure 8E). They showed that the wall thickness, diameter, and mechanical properties can be well tuned by tailoring the length of the hydrophobic pNbpm block. They also demonstrated that the nanotubes containing ionic pNce block can undergo a pH-

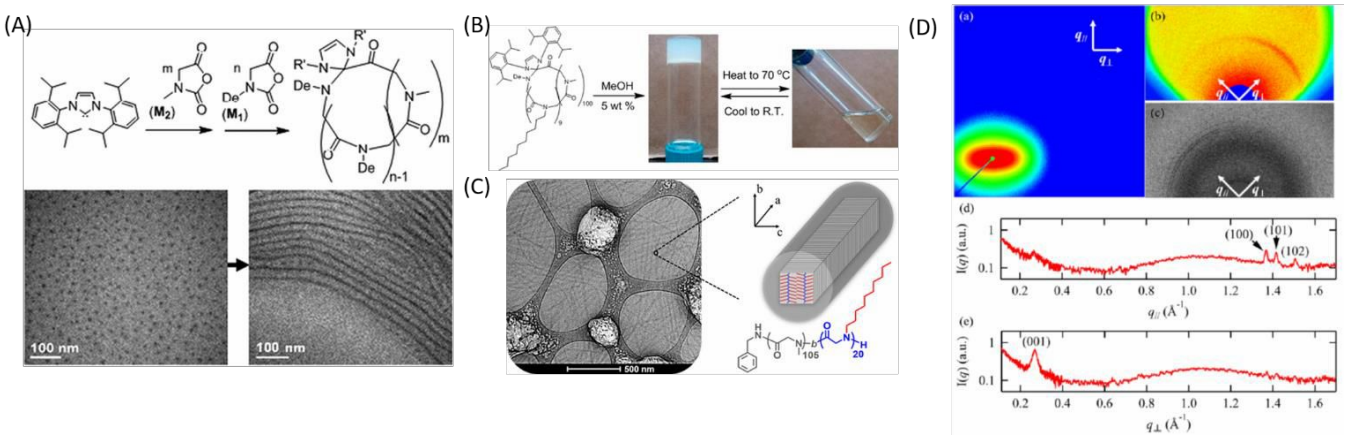

Figure **9**. Self-assembly of diblock copolypeptoids into crystalline cylindrical micelles. (A) Chemical structure of cyclic diblock copolypeptoid c-PNMG-PNDG and cryo-TEM images showing the transition from spherical micelles to long cylindrical micelles. Reprinted with permission from Ref. [61]. Copyright (2011) American Chemistry Society. (B) The c-PNMG-PNDG showed thermal reversible gelation in MeOH. Reprinted with permission from Ref. [74]. Copyright (2013) American Chemistry Society. (C) CryoTEM image of cylindrical micelles formed by linear diblock copolypeptoids l-PNMG-PNDG and the proposed model of cylindrical micelles. (D) Two-dimensional (a) SAXS, (b) MAXS, and (c) WAXS images for 5 mg/mL PNMG105-b-PNDG20 in diluted methanol solution measured during a unidirectional flow at room temperature. The directions parallel (q∥) and perpendicular (q⊥) to the flow direction are indicated by arrows. The corresponding one-dimensional profiles of the MAXS/WAXS results along the q∥ and q⊥ directions are plotted in (d) and (e), respectively. (C) and (D). Reprinted with permission from Ref. [75]. Copyright (2019) American Chemistry Society.

triggered and reversible contraction-expansion motion. They further demonstrated that functional moieties can be precisely incorporated into nanotubes without disrupting the structure, making the nanotubes a robust platform to develop biomimetic nanomaterials for specific applications.

3.2 Diblock copolypeptoids synthesized by solution polymerization method

High molecular weight diblock copolypeptoids with various compositions can be approached by ring-opening polymerizations of R-NCAs using different monomer to initiator feed ratios. Zhang *et al*. reported that the cyclic diblock copolypeptoid poly(*N*-methyl glycine)-*b*-poly(*N*-decyl glycine) (*c*-pNMG$_{105}$-*b*-pNDG$_{10}$) self-assembled into amorphous spherical micelles that reorganized into micrometer-long crystalline cylindrical micelles of uniform diameter (12.5±1.7 nm) in methanol upon cooling to room temperature from heated solution (Figure 9A).[61] They attributed the morphology transition to the crystallization of the PNDG block, the core of the cylindrical micelles. The corresponding linear analogue (*l*-pNMG$_{112}$-*b*-pNDG$_{16}$) showed an identical morphological transition, which occurs more rapidly than for the cyclic polypeptoids presumably due to the faster crystallization of pNDG in the former. They further reported that these *c*- and *l*-pNMG-*b*-pNDG formed thermoreversible gel in methanol at higher concentrations (5-10 wt%) due to the entanglement of the crystalline cylindrical micelles (Figure 9B).[74] The gel-to-sol transition at the elevated temperature is attributed to the melting of the crystalline pNDG domains. The cyclic polymer gels exhibited higher gel-to-sol transition temperature and enhanced mechanical strength than that of linear analogues presumably due to the enhanced crystallinity of the fibrillar network in the former relative to the latter. They further investigated the arrangement of the crystalline domains inside the cylindrical micelles using X-ray/neutron solution scattering in conjunction with cryo-TEM.[75] Interestingly, the pNDG blocks were stacked in a face-to-face fashion along the long axis of the cylindrical micelles, as evidenced by the anisotropic neutron scattering peaks under a unidirectional flow in a capillary flow cell (Figures 9C and D). The crystal packing of the cylindrical micelles is different than that of the nanotubes reported by Sun *et al*.[52] in which the side-to-side packing of pNDG blocks were clearly observed along the long axis of the nanotubes by cryo-TEM (Figures 3E and F). They also studied the effect of polymer composition on the assembled structure and morphology of linear pNMG-*b*-pNDG. The self-assembled structure in methanol was found to change from 1D crystalline cylindrical micelles to rigid short nanorods and then 2D nanosheets as the volume fraction of pNDG block was increased from 0.44 to 0.61 and 0.68. In contrast to the nanosheets reported by Sun *et al*. in which the face-to-face packing of pNDG block was along the length of the nanosheets[72], the nanosheets in this study indicated that the face-to-face packing was along the width based on the barely discernible X-ray scattering along the face-to-face packing. The different crystal packing of pNDG block in the polydisperse system (pNMG-*b*-pNDG) and the nearly monodisperse system (pNDG-*b*-pNte) raises new questions about the chain length, block ratio and polydispersity in the crystallization of diblock copolymers.

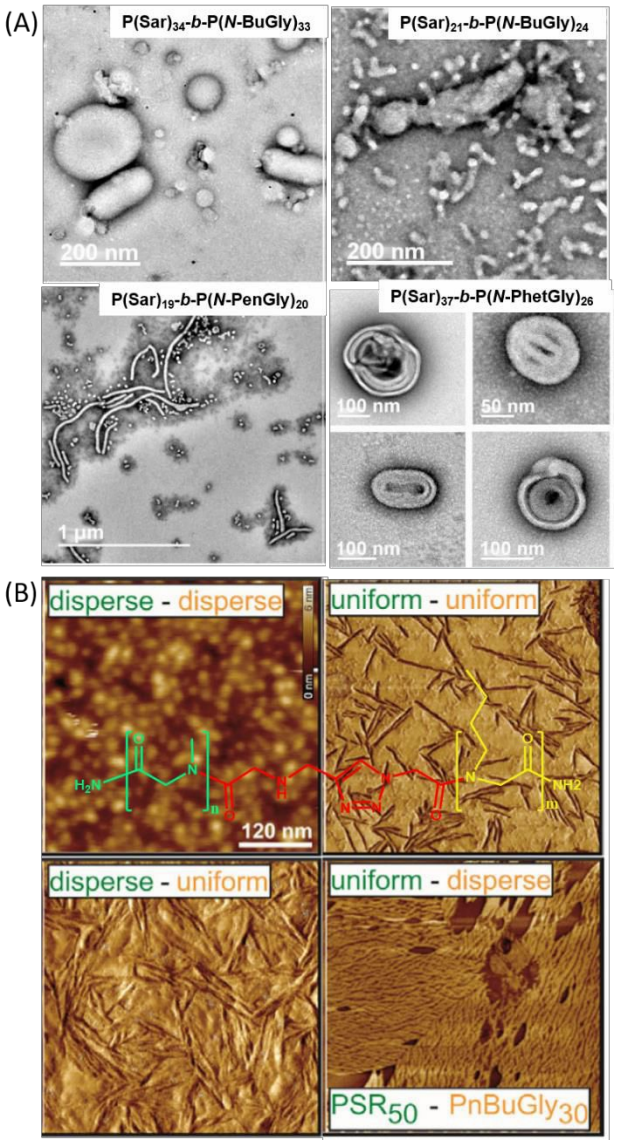

Figure **10**. Self-assembled structure of diblock copolypeptoids impacted by preparation method, polymer composition and molecular weight dispersity. (A) TEM images of assembled structures ranging from vesicles to worm-like micelles depending on the preparation method and polymer composition. Adapted from Ref. [78] under CC BY. (B) AFM images of assembled structures of diblock copolypeptoids with uniform or disperse blocks. Reprinted with permission from Ref. [79]. Copyright 2019 John Wiley and Sons

Luxenhofer *et al*. studied the self-assembly behavior of a series of amphiphilic diblock copolypeptoids bearing a hydrophilic pSar and an aliphatic block with ethyl, propyl, butyl or pentyl side chains in both water and PBS. They found that the tendency to form micelles increased with increasing hydrophobicity of the side chains.[76] Schlaad *et al*. found that aqueous solutions of the thermoresponsive-hydrophilic poly(*N*-(n-propyl)glycine)-*b*-pSar exhibited two cloud points at T_{cp}~30 and 45°C and a clearing point in between at T_{cl}~42°C.[77] Temperature-

dependent DLS experiments suggested that single molecules assembled into large structures above the first T_{cp} (~30) which disassembled into small micelle-like structures at T_{cl} (~42 °C) followed by re-aggregating into large sizes upon further heating. Luxenhofer *et al*. also studied the influence of block composition, chain-length heterogeneity, as well as the preparation method on the self-assembled structure of diblock copolypeptoids by dynamic light scattering (DLS) and TEM.[78] A wide range of morphologies, including micelles, interconnected worms, vesicles and onion-like vesicles, were formed depending on the hydrophilic block volume fraction, hydrophobic building blocks (aliphatic or aromatic), and preparation method (Figure 10A). However, precipitation to different extent was observed and the assembled structures were generally not uniform. Self-assembly behaviour of diblock copolypeptoids were not only dependent on the block composition and preparation method Luxenhofer *et al.* demonstrated that the dispersity also plays a major role in microphase separation and self-assembly of diblock copolypeptoids.[79] It appears that uniform hydrophobic blocks form more ordered structures compared to the dispersed analogues. They synthesized both hydrophobic pNBG and hydrophilic pNMG peptoids *via* solid-phase synthesis (uniform) and ring-opening polymerization (disperse). Then they coupled the pNBG and pNMG blocks, either uniform or disperse, using copper(I)-catalyzed azide-alkyne cycloaddition (CuAAC) to obtain the same amphiphilic diblock copolypeptoids of different chain length dispersity (Figure 10B). The diblock copolypeptoids with a uniform pNBG segment formed more ordered fiber-like micelles while the ones containing a disperse pNBG block formed ether spherical or leaf-like micelles (Figure 10B).

4. Biological applications

Polypeptoids, as a bioinspired and biomimetic material, have shown promise in a variety of biological applications. Several review articles focusing on the applications of polypeptoids in biomedicine and nanotechnology have been published in recent years.[35, 36] Diblock copolyepeptoids, which can self-assemble into various structures, have attracted increasing attention to explore their potential use as drug delivery vehicles, anti-cancer therapeutics, and imaging probes etc. Zhang *et al*. reported a reduction-responsive core-crosslinked spherical micelles based on amphiphilic diblock copolypeptoids as potential smart drug carriers.[16] The diblock copolypeptoids, consisting of a hydrophilic poly(*N*-ethyl glycine) (pNeh) block and a hydrophobic poly((*N*-propargyl glycine)-*random*-(*N*-decyl glycine)) block ($pNEG_{204}$-*b*-p($NPgG_{13}$-*r*-NDG_{15})), were synthesized by sequential ROP of the corresponding monomers (Figure 11A). They formed uniform spherical micelles in aqueous solutions which could be further crosslinked with a disulfide-containing diazide crosslinker to enhance the stability by copper mediated alkyne-azide cycloaddition (CuAAC) (Figure 11A). The core-crosslinked micelles showed enhanced loading capacity and loading efficiency of doxorubicin (DOX), an anticancer drug, compared to the non-crosslinked ones. The controlled release of DOX from the core-crosslinked micelles could be triggered by dissociation of the micelles upon addition of the reducing agent dithiothreitol, as evidenced by a combination of fluorescence spectroscopy, size exclusion chromatography (SEC), and ^{1}H NMR spectroscopy. The DOX released was able to inhibit the proliferation of HepG2 cancer cells in a concentration and time dependent manner, further demonstrating the controlled release of DOX in the cellular environment. Li and Ling *et al*. recently reported an oxidation-responsive polymersome system that may find applications in drug delivery[14]. The polymersomes were made from a diblock copolypeptoid, poly(*N*-3-(methylthio)propyl glycine)-*b*-polysarcosine ($pMeSPG_{60}$-*b*-$pSar_{50}$), prepared by ROP of thecorresponding *N*-substituted *N*-thiocarboxyanhydride (R-NTA). (Figure 11B). The polymersomes were shown to be ruptured by the action of reactive oxygen species (ROS) coming from added hydrogen peroxide, or singlet oxygen generated by light-activation of the encapsulated TPP photosensitizer (Figure 11B). The rupture of micelles, attributed to the oxidation of the hydrophobic thioether to hydrophilic sulfoxide side chains, was verified by confocal laser scanning microscopy showing the gradual disappearance of the vesicles, and by DLS which showed a decreased concentration and size of the micelle solutions. Despite the report of various therapeutic nanocarriers, the efficient intracellular delivery of them into the cytosol remains a challenge due to their tendency to be entrapped within membrane-bounded endosomes during endocytosis pathway and subsequent degradation.[80, 81] Lin and Chen *et al*. found that

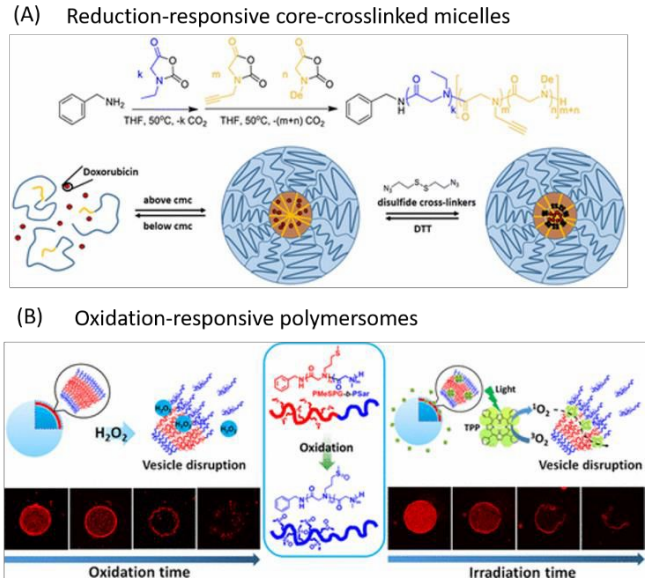

Figure **11**. Smart polypeptoid micelles showing potential as drug carriers. (A) Structure of diblock copolypeptoids PNEG-b-P(NPgG-r-NDG). The cartoon showed the formation of non-crosslinked micelles and the reduction-responsive core-crosslinked micelles. Reprinted with permission from Ref. [16]. Copyright (2016) American Chemistry Society. (B) Oxidation-responsive vesicles. The cartoon showed the rupture of the vesicles under oxidative environment upon addition of H_2O_2 or light-activation of the encapsulated TPP. Reprinted with permission from Ref. [14]. Copyright (2019) American Chemistry Society.

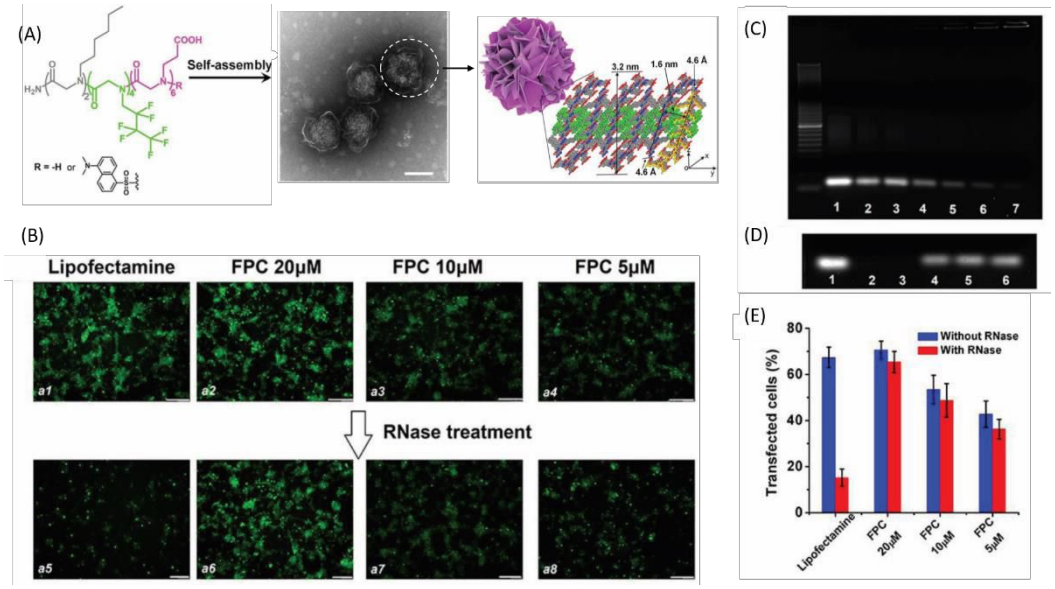

Figure **12**. Efficient gene transfection using crystalline nanoflowers, fluorinated peptoid crystal (FPC). (A) Chemical structures of amphiphilic fluorinated peptoids and schematic representation showing the self-assembly of the peptoids into crystalline nanoflower-like particles composed of bilayer-like packing of peptoids. (B) Representative confocal images of EGFP gene expression in H1299 cells mediated by top: from left to right; Lipofectamine (a1), FPC 20 μM (a2), FPC 10 μM (a3), FPC 5 μM (a4), and corresponding formulations after RNase treatment (a5–a8). (C) Gel-retardation assay of FPC/mRNA-EGFP at different ratios. Lane 1: mRNA only (0.5 μg); Lane 2: mRNA treated with FPC of 0.5 μM; line 3: mRNA treated with FPC of 1 μM; line 4: mRNA treated with FPC of 2.5 μM; line 5: mRNA treated with FPC of 5 μM; line 6: mRNA treated with FPC of 10 μM; line 7: mRNA treated with FPC of 20 μM. (D) Protection of mRNA from RNase digestion as evaluated by electrophoresis. (E) mRNA-EGFP expression determined by flow cytometry of FPC and a commercial product Lipofectamine without and with RNase treatment. Adapted with permission from Ref. [15]. Copyright 2018 John Wiley and Sons

peptoid nanocarriers showed highly efficient cytosolic delivery with minimal cytotoxicity. They reported a fluorinated amphiphilic sequence-defined diblock copolypeptoid which self-assembled into crystalline nanoflowers with structurally ordered surface, referred to as fluorinated peptoid crystal (FPC), composed of layers of crystalline bilayer nanosheets (Figure 12A).[15] They showed that the FPCs facilitated efficient cellular uptake, endosomal escape, and cytosolic delivery of ss DNA and mRNA, leading to successful intracellular gene expression and high transfection efficiency. Upon incubation of cells with the fluorescently-labelled FPC, most of the FPC were found beyond the plasma membrane as evidenced by the internal reflection fluorescence microscopy analysis, indicating the deep uptake within the cytosol. They also showed that these FPC enabled strong binding affinity toward ssDNA and mRNA (Figure 12C). The strong binding of mRNA to the FPC allowed effective protection of mRNA against nuclease degradation compared to the commercial transfection agent Lipofectamine (Figures 12B and D). They further demonstrated the excellent mRNA transfection performance mediated by the FPC/mRNA complex in H1299 cells and A549 adenocarcinoma human alveolar basal epithelial cells. The transfection efficiency reached as high as 71% at a concentration of 20 μM FPC, which is higher than that of using Lipofectamine Messenger MAX in H1299 cells (Figure 12E).

Similar to spherical micelles or vesicles, nanotubes have also found utility in a broad range of biological applications such as bioimaging, biosensing, drug delivery and anti-cancer therapy.[82-84] Lin and Chen *et al*. showed the potential of polypeptoid nanotubes for targeted tumor cell imaging and chemo-photodynamic therapy.[28] The nanotubes were made from amphiphilic diblock copolypeptoids, poly(*N*-(2-carboxyethyl)glycine)-*b*-poly(*N*-(4-bromophenyl)methyl glycine) (pNce-*b*-pNbpm), with functional groups Folic acid (FA) or Dansyl (DNS) covalently tagged at the *N*-terminus, adapted from previously reported nanotubes[55] (Figure 13A). Folic acid (FA) is known as an efficient ligand to specifically recognize FA receptors-overexpressed cells. Dansyl (DNS) exhibiting green fluorescence was incorporated for imaging purpose. Meso-tetrakis(4-carboxylphenyl)porphyrin (TCPP) is a well-known commercially available photosensitizer for photodynamic therapy (PDT). FA-tagged diblock copolypeptoids (Pep-FA) were coassembled with Pep-DNS or Pep-TCPP in a molar ratio of 1:1 to obtain nanotubes PepTs1 and PepTs2, respectively, for targeted imaging and PDT (Figure 13A). The FA-tagged nanotubes exhibited effective targeting on FA receptor-overexpressed H1299 cells compared to that on FA-negatively expressed A549 cells, indicating the highly specific recognitions between FA-tagged nanotubes and FA receptors of the cells. The PepTs1 nanotubes were further loaded with antitumor drug doxorubicin (DOX) for drug delivery and monitoring the intracellular drug release. (Figure 13B). PepTs1 nanotubes showed high drug loading efficiency (30%) and time-dependent and sustainable DOX release in cells. The TPP-functionalized PepTs2 nanotubes exhibited high phototoxicity against the cells upon exposed to irradiation at 660 nm, as shown by the bright red fluorescence emission of the PI stained dead cells in Figure 13C. PepTs2 nanotubes were further loaded with DOX for a binary anti-cancer methodology, the chemo-photodynamic therapy. The DOX loaded PepTs2 nanotubes have high killing

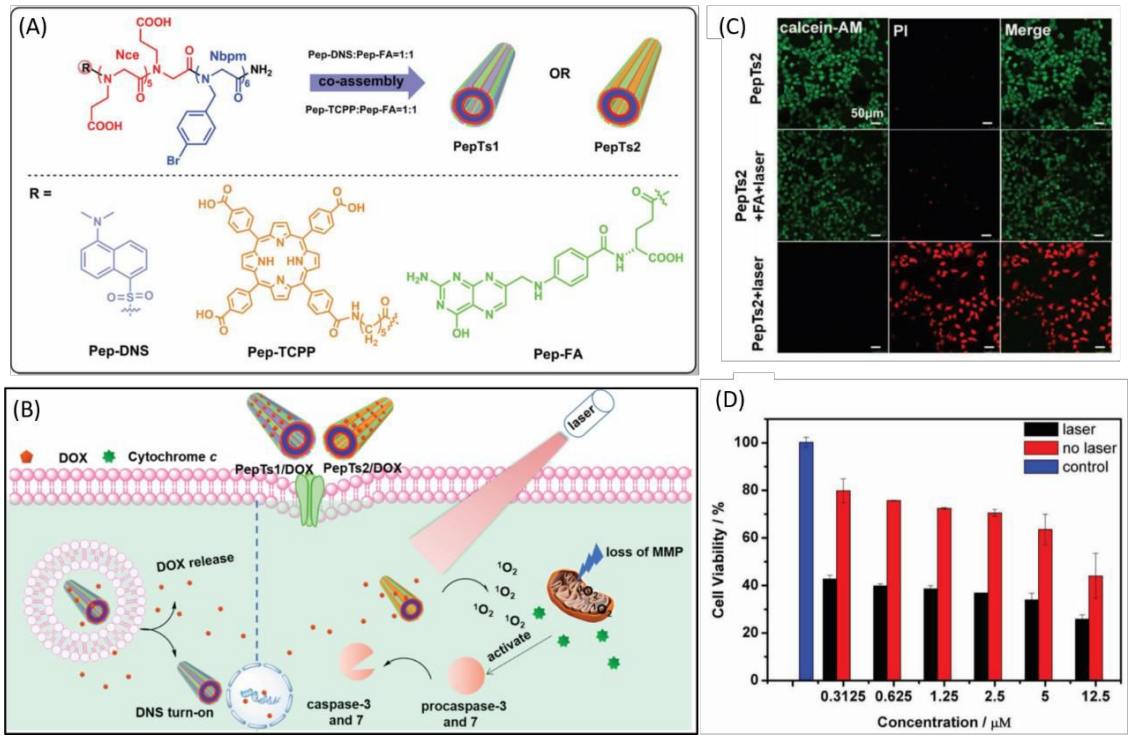

Figure **13**. Peptoid nanotubes for targeted imaging and chemo-photodynamic therapy. (A) Chemical structure of ligand-tagged $Nbpm_6$-Nce_6 peptoids and their assembly into crystalline nanotubes. PepTs1 formed by Pep-FA coassembled with Pep-DNS at a ratio of 1:1. PepTs2 formed by Pep-FA coassembled with Pep-TCPP at a ratio of 1:1. b) TEM images of PepTs2. (B) The endocytosis process of PepTs1 as platform to deliver DOX to H1299 cells, and activation of the apoptosis pathway caused by PepTs2 in H1299 cells. (C) live/dead cell images by PI/ calcein AM double staining. The laser irradiation power was 660 nm 500 mW cm−2 for 2 min. (D) MTT assay of the cytotoxicity of PepTs2/DOX against H1299 cells with/without irradiation at power of 500 mW cm−2 for 5 min. Adapted with permission from Ref. [28]. Copyright 2019 John Wiley and Sons.

efficiency toward H1299 cells due to the combined chemo-photodynamic therapy upon treatment with light irradiation (Figure 13D). These findings indicated that polypeptoid nanotubes are promising candidates for targeted tumor cell imaging and chemo-photodynamic therapy.

Conclusions and outlook

Polypeptoids, as a bioinspired and non-natural biomaterial, have increasing interest in the materials chemistry community due to their unique properties such as facile synthesis, biocompatibility, and enhanced proteolytic stability. The diblock copolypeptoids have shown great promise as a biomimetic platform for the design of nanomaterials that rival the structural complexity found in nature. The advances in the development of both solution polymerization methods and submonomer solid-phase synthesis methods have enabled access to a variety of well-defined diblock copolypeptoids, setting the stage for the development of polypeptoid materials for a wide variety of biomedical and biotechnological applications. The microphase separation and crystallization capability of diblock copolypeptoids have resulted diverse self-assembled nanostructures including spherical and cylindrical micelles, vesicles, nanotubes, nanosheets and nanoflowers for the potential use as drug and gene delivery vehicles, imaging, and anticancer agents. Those nanostructures may also find applications in biosensing, biodetection, and nano/microreactors due to the chemical and enzymatic stability of peptoids. There are so many design possibilities for peptoid structures due to the various synthetic methods developed. One can make 100mers with hundreds of possible choices for each position. Therefore, there are new opportunities to explore the impact of sequence-control in polymer science and to atomically engineer functional peptoid nanostructures. The advances in characterization technology (e.g., X-ray scattering and cryo-TEM etc.) and computational tools have provided access to the understanding of the molecular and atomic structure, and assembly mechanism of the self-assembled nanostructures. The future challenge is the understanding of the atomic structure and assembly rules of the nanoarchitectures to design polypeptoids nanomaterials with enhanced complexity and functionality more precisely and predictively.

Conflicts of interest

There are no conflicts to declare.

Acknowledgements

Primary funding for this work was provided by the Soft Matter Electron Microscopy Program (KC11BN), supported by the Office of Science, Office of Basic Energy Science, US Department of Energy, under Contract DE-AC02-05CH11231.

References

1. J. Sun and R. N. Zuckermann, *ACS Nano*, 2013, **7**, 4715-4732.
2. B. A. Chan, S. Xuan, A. Li, J. M. Simpson, G. L. Sternhagen, T. Yu, O. A. Darvish, N. Jiang and D. Zhang, *Biopolymers*, 2018, **109**, e23070.
3. A. Battigelli, *Biopolymers*, 2019, **110**, e23265.
4. R. Luxenhofer, C. Fetsch and A. Grossmann, *J. Polym. Sci., Part A: Polym. Chem.*, 2013, **51**, 2731-2752.
5. D. Zhang, S. H. Lahasky, L. Guo, C.-U. Lee and M. Lavan, *Macromolecules*, 2012, **45**, 5833-5841.
6. C. Secker, S. M. Brosnan, R. Luxenhofer and H. Schlaad, *Macromol. Biosci.*, 2015, **15**, 881-891.
7. A. Battigelli, J. H. Kim, D. C. Dehigaspitiya, C. Proulx, E. J. Robertson, D. J. Murray, B. Rad, K. Kirshenbaum and R. N. Zuckermann, *ACS Nano*, 2018, **12**, 2455-2465.
8. J. H. Kim, S. C. Kim, M. A. Kline, E. M. Grzincic, B. W. Tresca, J. Cardiel, M. Karbaschi, D. C. Dehigaspitiya, Y. Chen, V. Udumula, T. Jian, D. J. Murray, L. Yun, M. D. Connolly, J. Liu, G. Ren, C.-L. Chen, K. Kirshenbaum, A. R. Abate and R. N. Zuckermann, *ACS Nano*, 2019, DOI: 10.1021/acsnano.9b07498.
9. D. J. Murray, J. H. Kim, E. M. Grzincic, S. C. Kim, A. R. Abate and R. N. Zuckermann, *Langmuir*, 2019, **35**, 13671-13680.
10. G. K. Olivier, A. Cho, B. Sanii, M. D. Connolly, H. Tran and R. N. Zuckermann, *ACS Nano*, 2013, **7**, 9276-9286.
11. J. H. Kim, E. M. Grzincic, L. Yun, R. K. Spencer, M. A. Kline and R. N. Zuckermann, *Soft Matter*, 2020, DOI: 10.1039/C9SM01908A.
12. H. Jin, F. Jiao, M. D. Daily, Y. Chen, F. Yan, Y.-H. Ding, X. Zhang, E. J. Robertson, M. D. Baer and C.-L. Chen, *Nat. Commun.*, 2016, **7**, 12252.
13. F. Jiao, Y. Chen, H. Jin, P. He, C.-L. Chen and J. J. De Yoreo, *Adv. Funct. Mater.*, 2016, **26**, 8960-8967.
14. Y. Deng, H. Chen, X. Tao, F. Cao, S. Trépout, J. Ling and M.-H. Li, *Biomacromolecules*, 2019, **20**, 3435-3444.
15. Y. Song, M. Wang, S. Li, H. Jin, X. Cai, D. Du, H. Li, C.-L. Chen and Y. Lin, *Small*, 2018, **14**, 1803544.
16. A. Li and D. Zhang, *Biomacromolecules*, 2016, **17**, 852-861.
17. L. Zhu, J. M. Simpson, X. Xu, H. He, D. Zhang and L. Yin, *ACS Appl. Mater. Interfaces*, 2017, **9**, 23476-23486.
18. Y. Zhang, S. Xuan, O. Owoseni, M. Omarova, X. Li, M. E. Saito, J. He, G. L. McPherson, S. R. Raghavan, D. Zhang and V. T. John, *Langmuir*, 2017, **33**, 2780-2789.
19. J. M. V. Jun, M. V. P. Altoe, S. Aloni and R. N. Zuckermann, *Chem. Commun.*, 2015, **51**, 10218-10221.
20. S. Xuan, S. Gupta, X. Li, M. Bleuel, G. J. Schneider and D. Zhang, *Biomacromolecules*, 2017, **18**, 951-964.
21. D. L. Cheung and K. H. A. Lau, *Langmuir*, 2019, **35**, 1483-1494.
22. K. H. A. Lau, C. Ren, T. S. Sileika, S. H. Park, I. Szleifer and P. B. Messersmith, *Langmuir*, 2012, **28**, 16099-16107.
23. K. H. A. Lau, T. S. Sileika, S. H. Park, A. M. L. Sousa, P. Burch, I. Szleifer and P. B. Messersmith, *Advanced Materials Interfaces*, 2015, **2**, 1400225.
24. N. P. Chongsiriwatana, J. A. Patch, A. M. Czyzewski, M. T. Dohm, A. Ivankin, D. Gidalevitz, R. N. Zuckermann and A. E. Barron, *Proc. Natl. Acad. Sci.*, 2008, **105**, 2794-2799.
25. B. Mojsoska, R. N. Zuckermann and H. Jenssen, *Antimicrob. Agents Chemother.*, 2015, **59**, 4112-4120.
26. A. M. Czyzewski, H. Jenssen, C. D. Fjell, M. Waldbrook, N. P. Chongsiriwatana, E. Yuen, R. E. W. Hancock and A. E. Barron, *PLoS One*, 2016, **11**, e0135961.
27. L. Chio, J. T. Del Bonis-O'Donnell, M. A. Kline, J. H. Kim, I. R. McFarlane, R. N. Zuckermann and M. P. Landry, *Nano Lett.*, 2019, **19**, 7563-7572.
28. Y. Luo, Y. Song, M. Wang, T. Jian, S. Ding, P. Mu, Z. Liao, Q. Shi, X. Cai, H. Jin, D. Du, W.-J. Dong, C.-L. Chen and Y. Lin, *Small*, 2019, **15**, 1902485.
29. A. I. Nguyen, R. K. Spencer, Christopher L. Anderson and R. N. Zuckermann, *Chemical Science*, 2018, **9**, 8806-8813.
30. S. Xuan, C.-U. Lee, C. Chen, A. B. Doyle, Y. Zhang, L. Guo, V. T. John, D. Hayes and D. Zhang, *Chem. Mater.*, 2016, **28**, 727-737.
31. N. Gangloff, J. Ulbricht, T. Lorson, H. Schlaad and R. Luxenhofer, *Chem. Rev.*, 2016, **116**, 1753-1802.
32. R. N. Zuckermann, *Pept. Sci.*, 2011, **96**, 545-555.
33. J. Ulbricht, R. Jordan and R. Luxenhofer, *Biomaterials*, 2014, **35**, 4848-4861.
34. R. Hoogenboom and H. Schlaad, *Polymer Chemistry*, 2016, DOI: 10.1039/C6PY01320A.
35. J. Sun and Z. Li, in *Peptide Applications in Biomedicine, Biotechnology and Bioengineering*, ed. S. Koutsopoulos, Woodhead Publishing, 2018, DOI: https://doi.org/10.1016/B978-0-08-100736-5.00007-7, pp. 183-213.
36. K. H. A. Lau, *Biomaterials Science*, 2014, **2**, 627-633.
37. A. M. Rosales, R. A. Segalman and R. N. Zuckermann, *Soft Matter*, 2013, **9**, 8400-8414.
38. A. M. Rosales, B. L. McCulloch, R. N. Zuckermann and R. A. Segalman, *Macromolecules*, 2012, **45**, 6027-6035.
39. W. van Zoelen, R. N. Zuckermann and R. A. Segalman, *Macromolecules*, 2012, **45**, 7072-7082.
40. W. van Zoelen, H. G. Buss, N. C. Ellebracht, N. A. Lynd, D. A. Fischer, J. Finlay, S. Hill, M. E. Callow, J. A. Callow, E. J. Kramer, R. N. Zuckermann and R. A. Segalman, *ACS Macro Letters*, 2014, **3**, 364-368.
41. C. Leng, H. G. Buss, R. A. Segalman and Z. Chen, *Langmuir*, 2015, **31**, 9306-9311.
42. A. L. Patterson, B. Wenning, G. Rizis, D. R. Calabrese, J. A. Finlay, S. C. Franco, R. N. Zuckermann, A. S. Clare, E. J. Kramer, C. K. Ober and R. A. Segalman, *Macromolecules*, 2017, **50**, 2656-2667.
43. A. L. Patterson, S. P. O. Danielsen, B. Yu, E. C. Davidson, G. H. Fredrickson and R. A. Segalman, *Macromolecules*, 2019, **52**, 1277-1286.
44. B. Yu, S. P. O. Danielsen, A. L. Patterson, E. C. Davidson and R. A. Segalman, *Macromolecules*, 2019, **52**, 2560-2568.
45. Z. Shi, Y. Wei, C. Zhu, J. Sun and Z. Li, *Macromolecules*, 2018, **51**, 6344-6351.
46. Y. Wei, J. Tian, Z. Zhang, C. Zhu, J. Sun and Z. Li, *Macromolecules*, 2019, **52**, 1546-1556.
47. R. N. Zuckermann, J. M. Kerr, S. B. H. Kent and W. H. Moos, *J. Am. Chem. Soc.*, 1992, **114**, 10646-10647.
48. H. K. Murnen, A. M. Rosales, J. N. Jaworski, R. A. Segalman and R. N. Zuckermann, *J. Am. Chem. Soc.*, 2010, **132**, 16112-16119.
49. J. Sun, A. A. Teran, X. Liao, N. P. Balsara and R. N. Zuckermann, *J. Am. Chem. Soc.*, 2013, **135**, 14119-14124.
50. J. Sun, X. Liao, A. M. Minor, N. P. Balsara and R. N. Zuckermann, *J. Am. Chem. Soc.*, 2014, **136**, 14990-14997.
51. J. Sun, A. A. Teran, X. Liao, N. P. Balsara and R. N. Zuckermann, *J. Am. Chem. Soc.*, 2014, **136**, 2070-2077.

52. J. Sun, X. Jiang, R. Lund, K. H. Downing, N. P. Balsara and R. N. Zuckermann, *Proc. Natl. Acad. Sci.*, 2016, **113**, 3954-3959.
53. J. Sun, X. Jiang, A. Siegmund, M. D. Connolly, K. H. Downing, N. P. Balsara and R. N. Zuckermann, *Macromolecules*, 2016, **49**, 3083-3090.
54. D. R. Greer, M. A. Stolberg, S. Xuan, X. Jiang, N. P. Balsara and R. N. Zuckermann, *Macromolecules*, 2018, **51**, 9519-9525.
55. H. Jin, Y.-H. Ding, M. Wang, Y. Song, Z. Liao, C. J. Newcomb, X. Wu, X.-Q. Tang, Z. Li, Y. Lin, F. Yan, T. Jian, P. Mu and C.-L. Chen, *Nat. Commun.*, 2018, **9**, 270.
56. G. L. Sternhagen, S. Gupta, Y. Zhang, V. John, G. J. Schneider and D. Zhang, *J. Am. Chem. Soc.*, 2018, **140**, 4100-4109.
57. C. Fetsch and R. Luxenhofer, *Macromol. Rapid Commun.*, 2012, **33**, 1708-1713.
58. C. Fetsch, A. Grossmann, L. Holz, J. F. Nawroth and R. Luxenhofer, *Macromolecules*, 2011, **44**, 6746-6758.
59. N. Gangloff, C. Fetsch and R. Luxenhofer, *Macromol. Rapid Commun.*, 2013, **34**, 997-1001.
60. B. A. Chan, S. Xuan, M. Horton and D. Zhang, *Macromolecules*, 2016, **49**, 2002-2012.
61. C.-U. Lee, T. P. Smart, L. Guo, T. H. Epps and D. Zhang, *Macromolecules*, 2011, **44**, 9574-9585.
62. A. Li, L. Lu, X. Li, L. He, C. Do, J. C. Garno and D. Zhang, *Macromolecules*, 2016, **49**, 1163-1171.
63. S. Wang, Y. Tao, J. Wang, Y. Tao and X. Wang, *Chemical Science*, 2019, **10**, 1531-1538.
64. H. K. Murnen, A. R. Khokhlov, P. G. Khalatur, R. A. Segalman and R. N. Zuckermann, *Macromolecules*, 2012, **45**, 5229-5236.
65. B.-C. Lee, R. N. Zuckermann and K. A. Dill, *J. Am. Chem. Soc.*, 2005, **127**, 10999-11009.
66. X. Jiang, R. K. Spencer, J. Sun, C. Ophus, R. N. Zuckermann, K. H. Downing and N. P. Balsara, *J. Phys. Chem. B*, 2019, **123**, 1195-1205.
67. C.-U. Lee, A. Li, K. Ghale and D. Zhang, *Macromolecules*, 2013, **46**, 8213-8223.
68. D. R. Greer, M. A. Stolberg, J. Kundu, R. K. Spencer, T. Pascal, D. Prendergast, N. P. Balsara and R. N. Zuckermann, *J. Am. Chem. Soc.*, 2018, **140**, 827-833.
69. E. Nogales and Sjors H. W. Scheres, *Mol. Cell*, 2015, **58**, 677-689.
70. Y. Cheng, *Cell*, 2015, **161**, 450-457.
71. X. Jiang, D. R. Greer, J. Kundu, C. Ophus, A. M. Minor, D. Prendergast, R. N. Zuckermann, N. P. Balsara and K. H. Downing, *Macromolecules*, 2018, **51**, 7794-7799.
72. X. Jiang, S. Xuan, J. Kundu, D. Prendergast, R. N. Zuckermann and N. P. Balsara, *Soft Matter*, 2019, **15**, 4723-4736.
73. S. Xuan, X. Jiang, R. K. Spencer, N. K. Li, D. Prendergast, N. P. Balsara and R. N. Zuckermann, *Proc. Natl. Acad. Sci.*, 2019, **116**, 22491-22499.
74. C.-U. Lee, L. Lu, J. Chen, J. C. Garno and D. Zhang, *ACS Macro Letters*, 2013, **2**, 436-440.
75. N. Jiang, T. Yu, O. A. Darvish, S. Qian, I. K. Mkam Tsengam, V. John and D. Zhang, *Macromolecules*, 2019, **52**, 8867-8877.
76. C. Fetsch, S. Flecks, D. Gieseler, C. Marschelke, J. Ulbricht, K.-H. van Pée and R. Luxenhofer, *Macromol. Chem. Phys.*, 2015, **216**, 547-560.
77. A. Bogomolova, C. Secker, J. Koetz and H. Schlaad, *Colloid. Polym. Sci.*, 2017, **295**, 1305-1312.
78. C. Fetsch, J. Gaitzsch, L. Messager, G. Battaglia and R. Luxenhofer, *Sci. Rep.*, 2016, **6**, 33491.
79. N. Gangloff, M. Höferth, V. Stepanenko, B. Sochor, B. Schummer, J. Nickel, H. Walles, R. Hanke, F. Würthner, R. N. Zuckermann and R. Luxenhofer, *Biopolymers*, 2019, **110**, e23259.
80. N. Kamaly, Z. Xiao, P. M. Valencia, A. F. Radovic-Moreno and O. C. Farokhzad, *Chem. Soc. Rev.*, 2012, **41**, 2971-3010.
81. C. M. Jewell, J.-M. Jung, P. U. Atukorale, R. P. Carney, F. Stellacci and D. J. Irvine, *Angew. Chem. Int. Ed.*, 2011, **50**, 12312-12315.
82. Z. Liu, S. Tabakman, K. Welsher and H. Dai, *Nano Res.*, 2009, **2**, 85-120.
83. R. de la Rica, E. Mendoza, L. M. Lechuga and H. Matsui, *Angew. Chem. Int. Ed.*, 2008, **47**, 9752-9755.
84. Q. Lu, D. Ericson, Y. Song, C. Zhu, R. Ye, S. Liu, J. A. Spernyak, D. Du, H. Li, Y. Wu and Y. Lin, *ACS Appl. Mater. Interfaces*, 2017, **9**, 23325-23332.

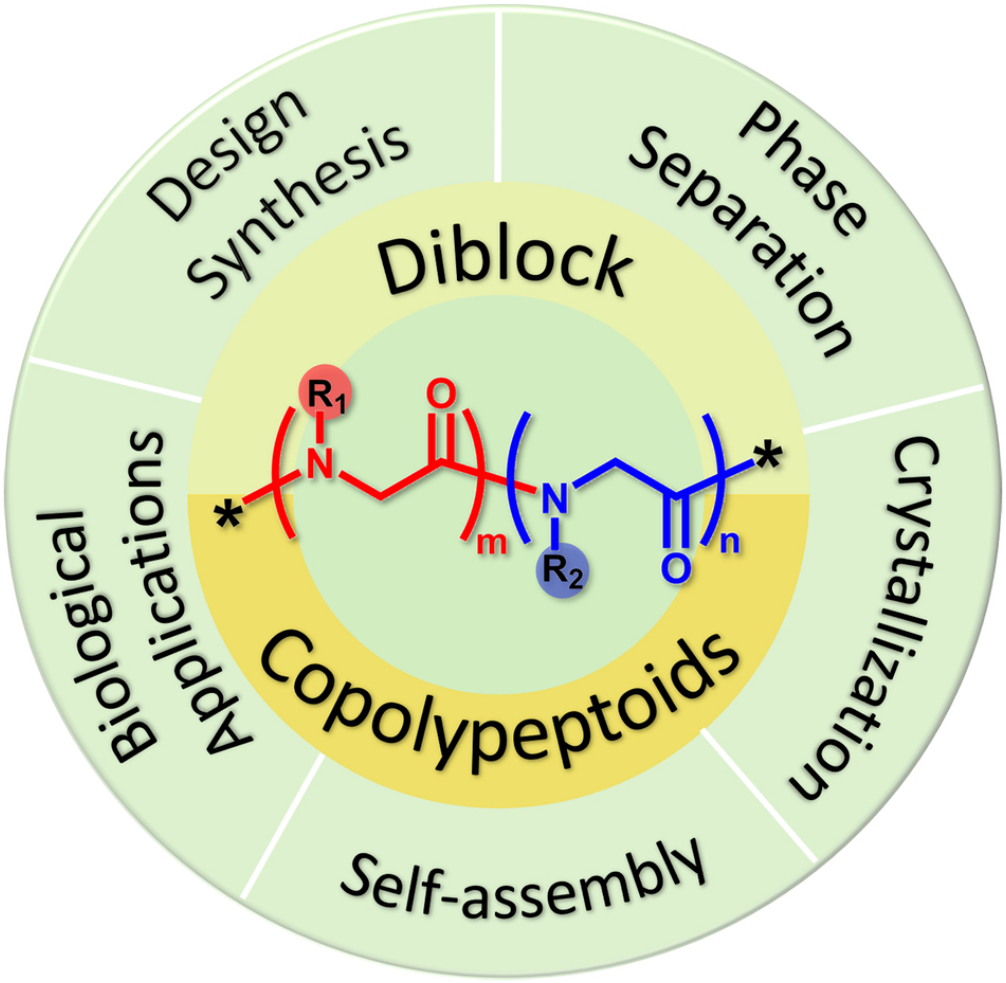

40x39mm (600 x 600 DPI)